

Geo-DefakeHop: High-Performance Geographic Fake Image Detection

Hong-Shuo Chen^{a,*}, Kaitai Zhang^a, Shuowen Hu^b, Suya You^b and C.-C. Jay Kuo^a

^aUniversity of Southern California, Los Angeles, California, USA

^bArmy Research Laboratory, Adelphi, Maryland, USA

ARTICLE INFO

Keywords:

Geo Artificial Intelligence (GeoAI)

Parallel Subspace Learning (PSL)

Generative Adversarial Network (GAN)

ABSTRACT

A robust fake satellite image detection method, called Geo-DefakeHop, is proposed in this work. Geo-DefakeHop is developed based on the parallel subspace learning (PSL) methodology. PSL maps the input image space into several feature subspaces using multiple filter banks. By exploring response differences of different channels between real and fake images for a filter bank, Geo-DefakeHop learns the most discriminant channels and uses their soft decision scores as features. Then, Geo-DefakeHop selects a few discriminant features from each filter bank and ensemble them to make a final binary decision. Geo-DefakeHop offers a light-weight high-performance solution to fake satellite images detection. Its model size is analyzed, which ranges from 0.8 to 62K parameters. Furthermore, it is shown by experimental results that it achieves an F1-score higher than 95% under various common image manipulations such as resizing, compression and noise corruption.

1. Introduction

Artificial intelligence (AI) and deep learning (DL) techniques have made significant advances in recent years by leveraging more powerful computing resources and larger collected and labeled datasets, creating breakthroughs in various fields such as computer vision, natural language processing, and robotics. Geospatial science (Janowicz, Gao, McKenzie, Hu and Bhaduri, 2020) and remote sensing (Ma, Liu, Zhang, Ye, Yin and Johnson, 2019) also benefit from this development, involving increased application of AI to process data arising from cartography and geographic information science (GIS) more effectively. Despite the countless advantages brought by AI, misinformation over the Internet, ranging from fake news (Radford, Wu, Child, Luan, Amodei, Sutskever et al., 2019) to fake images and videos (Dolhansky, Bitton, Pflaum, Lu, Howes, Wang and Ferrer, 2020; Zi, Chang, Chen, Ma and Jiang, 2020; Li, Yang, Sun, Qi and Lyu, 2020; Zhou, Wang, Liang and Shen, 2021; Rössler, Cozzolino, Verdoliva, Riess, Thies and Nießner, 2018; Jiang, Li, Wu, Qian and Loy, 2020), poses a serious threat to our society. It is important to be able to judge the authenticity of online content (FBI, 2019).

In the context of geospatial science, satellite images are utilized in various applications such as weather prediction, agriculture crops prediction, flood and fire control. If one cannot determine whether a satellite image is real or fake, it would be risky to use it for decision making. Fake satellite images have impacts on national security as well. For example, adversaries can create fake satellite images to hide important military infrastructure and/or create fake ones to deceive others. Though government analysts could verify the authenticity of geospatial imagery leveraging other satellites or data sources, this would be prohibitively time intensive. For the public, it would be extremely difficult to verify the authenticity of satellite images.

It is becoming easier and easier to generate realistically looking images due to the rapid growth of generative adversarial networks (GANs) (Brock, Donahue and Simonyan, 2018; Karras, Laine and Aila, 2019; Park, Liu, Wang and Zhu, 2019; Choi, Choi, Kim, Ha, Kim and Choo, 2018; Karras, Aila, Laine and Lehtinen, 2017; Zhu, Park, Isola and Efros, 2017). Typically, a base map of an input satellite image can be first produced by one GAN. Then, a fake satellite image can be generated by another GAN based on the base map. Since generated satellite images are difficult to discern by human eyes, there is an urgent need to develop an automatic detection system that can find fake satellite images accurately and efficiently.

Little research has been done on fake satellite images detection due to the lack of a proper fake satellite image dataset. The first fake satellite image dataset was recently proposed by Zhao *et al.* (Zhao, Zhang, Xu, Sun and Deng, 2021). Furthermore, handcrafted spatial, histogram, and frequency features were derived and a support vector machine (SVM) classifier was trained to determine whether a satellite tile is real and fake. It has an F1-score of 83% in detection performance. We are not aware of any DL solution to this problem yet but expect to see some in the future. There are DL-based fake image detection methods for other types of images. They will be reviewed in Sec. 2.

A robust fake satellite image detection method, called Geo-DefakeHop, is proposed in this work. Our research is based on one observation and one assumption. The observation is that the human visual system (HVS) (Hall and Hall, 1977) has its limitation. That is, it behaves like a low-pass filter and, as a result, it has a poor discriminant power for high-frequency responses. The assumption is that GANs can generate realistic images by reproducing low-frequency responses of synthesized images well. Yet, it might not be able to synthesize both low and high-frequency components well due to its limited model complexity. If this assumption holds, we can focus on differences between higher frequency components in differentiating true and fake images.

*Corresponding author

✉ hongshuo@usc.edu (H. Chen)

ORCID(s): 0000-0003-1116-939X (H. Chen)

This high-level idea can be implemented by a set of filters operating at all pixel locations in parallel, known as a filter bank in signal processing. Each filter offers responses of a particular frequency channel in the spatial domain and these responses can be used to check the discriminant power of a channel from the training data. To make the detection model more robust, we adopt multiple filter banks, find discriminant channels from each, and ensemble their responses to get the final binary decision. Since multiple filter banks are used simultaneously, it is named parallel subspace learning (PSL). The proposed Geo-DefakeHop offers a lightweight, high-performance and robust solution to fake satellite images detection. Its model ranges from 0.8 to 62K parameters. It achieves an F1-score higher than 95% under various common image manipulations such as resizing, compression and noise corruption.

The contributions of this work are summarized below.

1. We propose a fake satellite image detection method, called Geo-DefakeHop, which exploits the PSL methodology to extract discriminant features with the implementation of multiple filter banks.
2. We use the heat map to visualize prediction results and spatial responses of different frequency channels for Geo-DefakeHop's interpretability.
3. We conduct extensive experiments to demonstrate the high performance of Geo-DefakeHop and its robustness against various image manipulations.

The rest of this paper is organized as follows. Related work is reviewed in Sec. 2. The Geo-DefakeHop method is presented in Sec. 3. Experiments are shown in Sec. 4. Finally, concluding remarks are given in Sec. 5.

2. Related Work

2.1. Fake images generation

GANs provide powerful machine learning models for image-to-image translation. It consists of two neural networks in the training process: a generator and a discriminator. The generator attempts to generate fake images to fool the discriminator while the discriminator tries to distinguish generated fake images from real ones. They are jointly trained via end-to-end optimization with an adversarial loss. In the inference stage, only the generator is needed. For image-to-image translation, GANs need paired images to train, say, image A from source domain X and image B from target domain Y , where images A and B describe the same object or scene. This limits GAN's power since paired images are challenging to collect. Cycle-consistent GAN (CycleGAN) (Zhu et al., 2017) was proposed to overcome this difficulty. It learns to translate an image from source domain X to target domain Y without paired images. To achieve this, CycleGAN supplements the desired mapping, G , with an inverse mapping, F , which maps images in domain Y back to domain X . It imposes a cycle consistency loss to minimize the distance between $F(G(X))$ and X . CycleGAN has been applied to many applications, including

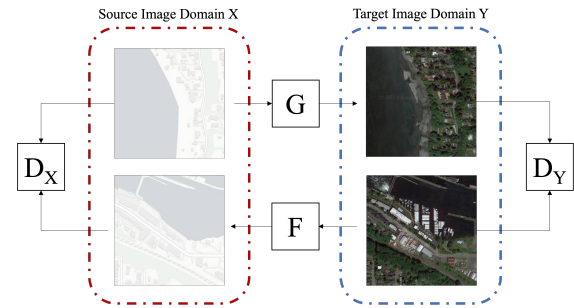


Figure 1: Illustration of CycleGAN and its application to fake satellite image generation.

fake satellite image generation (Zhao et al., 2021) as shown in Fig. 1, where a base map of an input satellite image is first generated by one GAN. Then, a fake satellite image is generated by another GAN based on the base map.

2.2. Fake images detection

Most fake image detection methods adopt convolution neural networks (CNNs). (Wang, Wang, Zhang, Owens and Efros, 2020) used the real and fake images generated by ProGAN (Karras et al., 2017) as the input of ResNet-50 pretrained by the ImageNet. (Zhang, Karaman and Chang, 2019) generated fake images with their designed GAN, called AutoGAN, and claimed that CNN trained by their simulated images could learn artifacts of fake images. (Nataraj, Mohammed, Manjunath, Chandrasekaran, Flenner, Bappy and Roy-Chowdhury, 2019) borrowed the idea from image steganalysis and used the co-occurrence matrix as input to a customized CNN so that it can learn the differences between real and fake images. By following this idea, (Barni, Kallas, Nowroozi and Tondi, 2020) added the cross-band co-occurrence matrix to the input so as to increase the stability of the model. (Guarnera, Giudice and Battiato, 2020) utilized the EM algorithm and the KNN classifier to learn the convolution traces of artifacts generated by GANs. Little research has been done to date on fake satellite images detection due to the lack of available datasets. (Zhao et al., 2021) proposed the first fake satellite image dataset with simulated satellite images from three cities (i.e., Tacoma, Seattle and Beijing). Furthermore, it used 26 hand-crafted features to train an SVM classifier for fake satellite image detection. The features can be categorized into spatial, histogram and frequency three classes. Features of different classes are concatenated for performance evaluation. In Sec. 4, we will benchmark our proposed Geo-DefakeHop method with the method in (Zhao et al., 2021).

2.3. PixelHop and Saab Transform

The PixelHop concept was introduced by Chen *et al.* in (Chen and Kuo, 2020). Each PixelHop has local patches of the same size as its input. Suppose that local patches are of dimension $L = s_1 \times s_2 \times c$, where $s_1 \times s_2$ is the spatial dimension and c is the spectral dimension. A PixelHop defines a mapping from pixel values in a patch to a set of spectral coefficients, which is called the Saab

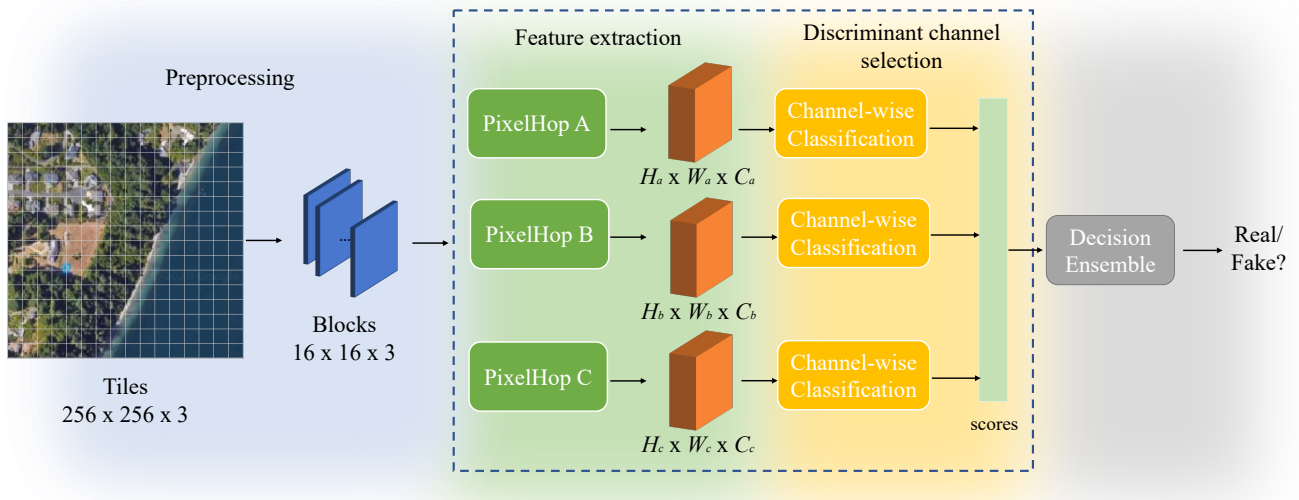


Figure 2: An overview of the Geo-DefakeHop method, where the input is an image tile and the output is a binary decision on whether the input is an authentic or a fake one. First, each input tile is partitioned into non-overlapping blocks of dimension $16 \times 16 \times 3$. Second, each block goes through one PixelHop or multiple PixelHops, each of which yields 3D tensor responses of dimension $H \times W \times C$. Third, for each PixelHop, an XGBoost classifier is applied to spatial samples of each channel to generate channel-wise (c/w) soft decision scores and a set of discriminant channels are selected accordingly. Last, all block decision scores are ensemble to generate the final decision of the image tile.

transform (Kuo, Zhang, Li, Duan and Chen, 2019). The Saab transform is a variant of the principal component analysis (PCA). For standard PCA, we subtract the ensemble mean and then conduct eigen-analysis on the covariance matrix of input vectors. The ensemble mean is difficult to estimate if the sample size is small. The Saab transform decomposes the n -dimensional signal space into a one-dimensional DC (direct current) subspace and an $(n - 1)$ -dimensional AC (alternating current) subspace. Signals in the AC subspace have an ensemble mean close to zero. Then, we can apply PCA to the AC signal and decompose it into $(n - 1)$ channels. Saab coefficients are unsupervised data-driven features since Saab filters are derived from the local correlation structure of pixels.

2.4. Differences between DefakeHop and Geo-DefakeHop

The Saab transform can be implemented conveniently with filter banks. It has been successfully applied to many application domains. Examples include (Chen, Rouhsedaghat, Ghani, Hu, You and Kuo, 2021; Zhang, Wang, Wang, Sohrab, Gabbouj and Kuo, 2021; Liu, Xing, Yang, Kuo, Babu, Fakhri, Jenkins and Woo, 2021; Zhang, You, Kadam, Liu and Kuo, 2020). Among them, DefakeHop (Chen et al., 2021) is closest to our current work. However, there are three main differences between DefakeHop and Geo-DefakeHop proposed here. First, DefakeHop was proposed to detect deepfake videos, where the main target is human faces. Here, our target is to detect fake satellite images. Since the targets are different, we need to tailor the current work accordingly. Second, DefakeHop used multi-stage cascaded PixelHop units to extract features from human eyes, nose and mouth regions. It focused on low-frequency channels and discarded

high-frequency channels. In contrast, we abandon multi-stage Saab transforms in cascade, and adopt multiple one-stage Saab transforms that operate in parallel. We show that high-frequency channels are more discriminant than low-frequency channels for fake image detection. Third, no image manipulation was tested in DefakeHop. The robustness issue is carefully examined in the current work. We compare the performance of DefakeHop and Geo-DefakeHop in Sec. 4 and show that Geo-DefakeHop outperforms DefakeHop by a significant margin.

3. Geo-DefakeHop Method

Our idea is motivated by the observation that GANs fail to generate high-frequency components such as edges and complex textures well. It is pointed out by (Frank, Eisenhofer, Schönherr, Fischer, Kolossa and Holz, 2020) that GANs have inconsistencies between the spectrum of real and fake images in high-frequency bands. Another evidence is that images generated by simple GANs are blurred and unclear. Blurry artifacts are reduced and more details are added by advanced GANs to yield higher quality fake images. Although these high quality simulated images look real to human eyes because of the limitation of the HVS, it does not mean that the high-frequency fidelity loss is not detectable by machines. Another shortcoming of generated images is periodic patterns introduced by convolution and deconvolution operations in GAN models as reported in (Guarnera et al., 2020). GANs often use a certain size of convolution and deconvolution filters (e.g., 3×3 or 5×5). They leave traces on simulated images in form of periodic patterns in some particular frequency bands. Sometimes, when GAN

models do not perform well, they can be observed by human eyes.

Being motivated by the above two observations, we proposed a new method for fake satellite image detection as shown in Fig. 2. It consists of four modules:

1. Preprocessing: Input image tiles are cropped into non-overlapping blocks of a fix size.
2. Joint spatial/spectral feature extraction via PixelHop: The PixelHop has a local patch as its input and applies a set of Saab filters to pixels of the patch to yield a set of joint spatial/spectral responses as features for each block.
3. Channel-wise classification, discriminant channels selection and block-level decision ensemble: We apply an XGBoost classifier to spatial responses of each channel to yield a soft decision, and select discriminant channels accordingly. Then, the soft decisions from discriminant channels of a single PixelHop or multiple PixelHops are ensembled to yield the block-level soft decision.
4. Image-level decision ensemble: Block-level soft decisions are ensembled to yield the image-level decision.

They are elaborated below.

3.1. Preprocessing

A color satellite image tile of spatial resolution 256×256 covers an area of one kilometer square as shown in the left of Figure 2. It is cropped into 256 non-overlapping blocks of dimension $16 \times 16 \times 3$, where the last number 3 denotes the R, G, B three color channels. Each block has homogeneous content such as trees, buildings, land and ocean.

3.2. Joint spatial/spectral feature extraction via PixelHop

As described in Sec. 2.3, a PixelHop has a local patch of dimension $L = s_1 \times s_2 \times c$ as its input, where s_1 and s_2 are spatial dimensions and c is the spectral dimension. For square patches, we have $s_1 = s_2 = s$. We set s to 2, 3, 4 in the experiments. Since the input has R, G, B three channels, $c = 3$.

The PixelHop applies L Saab filters to pixels in the local patch, including one DC filter and $(L - 1)$ AC filters, to generate L responses per patch. The AC filters are obtained via eigen-analysis of AC components. The mapping from L pixel values to L filter responses defines the Saab transform. Since the AC filters are derived from the statistics of the input, the Saab transform is a data-driven transform.

We adopt overlapping patches with stride equal to one. Then, for a block of spatial size 16×16 , we obtain $W \times H$ patches, where $W = 17 - s_1$ and $H = 17 - s_2$. As a result, the block output is a set of joint spatial/spectral responses of dimension $W \times H \times L$. To give an example, if the local patch size is $3 \times 3 \times 3 = 27$, the block output is a 3D tensor of dimension $14 \times 14 \times 27$. They are used as features to be fed to the classifier in the next stage.

3.3. Channel-wise classification, discriminant channels selection and block-level decision ensemble

For each channel in a block, we have one response from each local patch so that there are $W \times H$ responses in total. These responses form a feature vector, and samples from blocks of training real/fake images are used to train a classifier, leading to channel-wise classification. The classifier can be any one used in machine learning such as Random Forest, SVM, and XGBoost. In our experiments, the XGBoost classifier (Chen and Guestrin, 2016) is chosen for its high performance. XGBoost is a gradient-boosting decision tree algorithm that can learn a nonlinear data distribution efficiently.

To evaluate the discriminant power of a channel, we divide the training data into two disjoint groups: 1) data used to train the classifier, and 2) data used to validate the channel performance. The latter provides a soft decision score predicted by the channel-wise classifier. The channel-wise performance evaluation reflects the generation power of a GAN in various frequency bands. Some channels are more discriminant than others because of the poor generation power of the GAN in that frequency band. Selection of discriminant channels is based on the performance of the validation data.

We use an example to explain discriminant channel selection. It is a PixelHop of dimension $3 \times 3 \times 3$, which has 27 channels in total. The x-axis of Fig. 3 is the channel index and the y-axis is the energy percentage curve or the performance curve measured by the F1 score, where the F1 score will be defined in Sec. 4.2. In these plots, blue lines indicate that energy percentage of each channel while red, magenta and green lines represent the F1 scores of the train, validation and test data. We consider the following four settings.

1. Raw images

A higher frequency channel usually has a higher performance score as shown in Fig. 3a. Low-frequency channels are not as discriminant as high-frequency channels. It validates our assumption that the GANs fail to generate high-frequency components with high fidelity.

2. Image resizing

The input image is resized from 256×256 to 64×64 . As compared with the setting of raw images, the discriminant power of high-frequency channels degrades a little bit as shown in Fig. 3b. This is attributed to the fact that the down-sampling operation uses a low pass filter to alleviate aliasing. Despite the performance drop of each channel, the overall detection performance can be preserved by selecting more channels.

3. Additive Gaussian noise

Noisy satellite images are obtained by adding white Gaussian noise with $\sigma = 0.1$, where the dynamic range of the input pixel is $[0, 1]$. Thus, the relative noise level is high. We see from Fig. 3c that

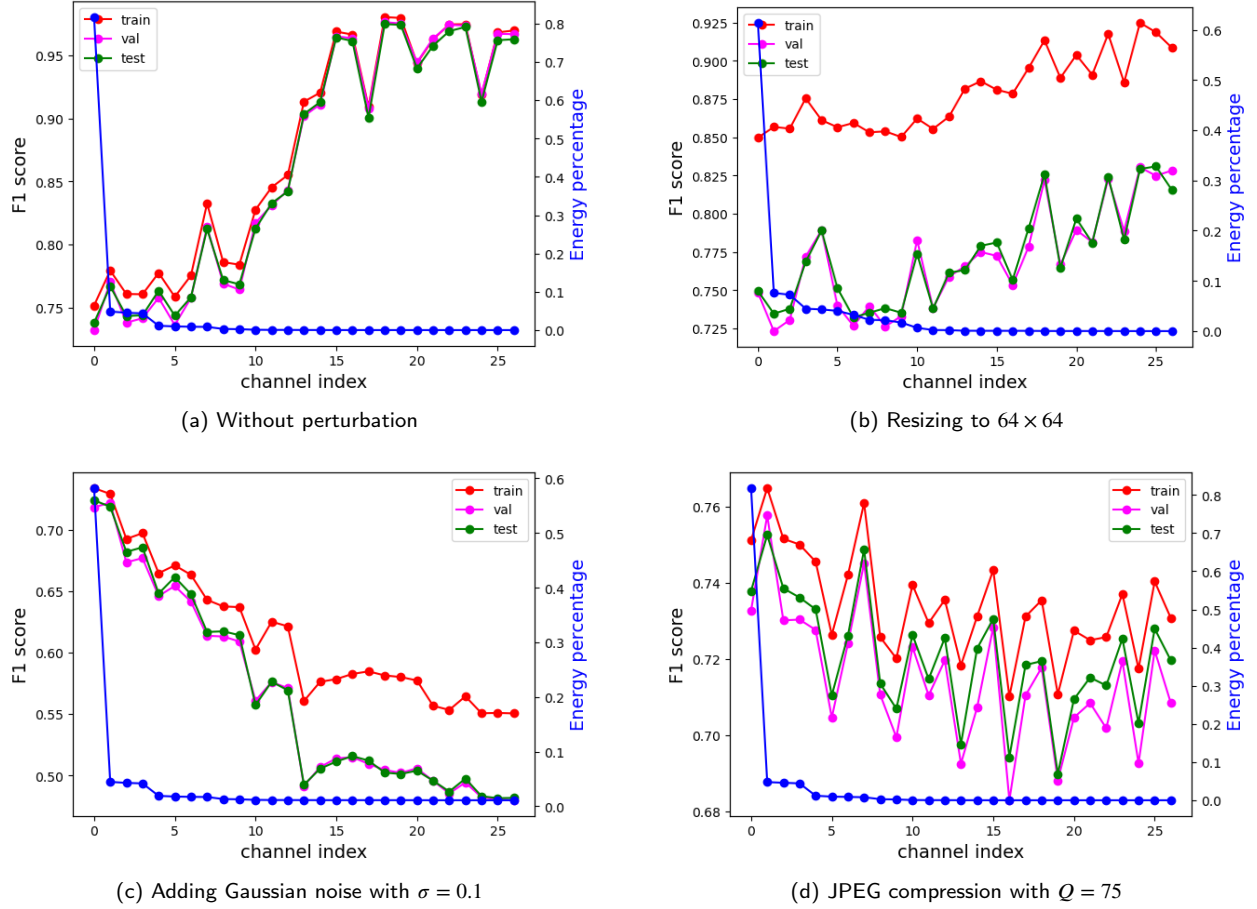


Figure 3: The channel-wise performance of four settings: a) without perturbation, b) resizing, c) adding Gaussian noise, and d) JPEG compression. The channel 0 is DC (Direct Current) and from the first channel to the 26th channel are corresponding to AC1 to AC26 (Alternating Current). The blue line is the energy percentage of each channel and the red, magenta and green lines are the F1-score of the training, validation and testing dataset. We observe that high-frequency channels without perturbation in 3a has a higher performance. After applying resizing, adding Gaussian noise and compression, the performance of high-frequency channels degrades as shown in 3b, 3c, 3d. The test score and validation score are closely related, indicating that the validation score can be used to select the discriminant channels.

low-frequency channels perform better than high-frequency channels. This is because we need to take the signal-to-noise ratio (SNR) into account. Low-frequency channels have higher SNR values than high-frequency ones. As a result, low-frequency channels have higher discriminant power.

4. JPEG compression

The experimental results with JPEG compression of quality factor 75 are shown in Fig. 3d. We see from the figure that the performance of different channels fluctuates. Generally, the performance of low-frequency channels is better than that of high-frequency channels since the responses of high-frequency channels degrade due to higher quantization errors in JPEG compression. However, We still can get discriminant channels based on the performance of the validation data.

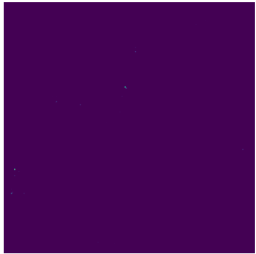
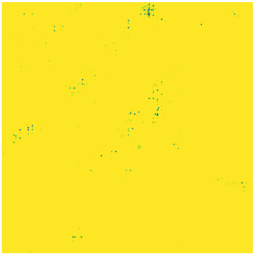
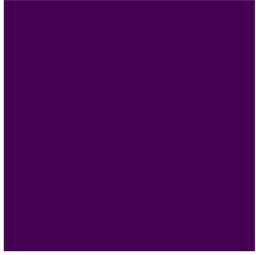
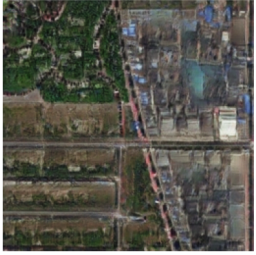
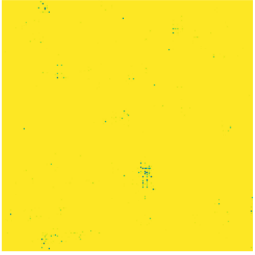
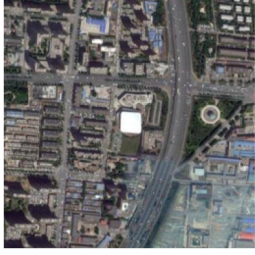
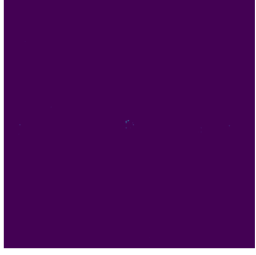
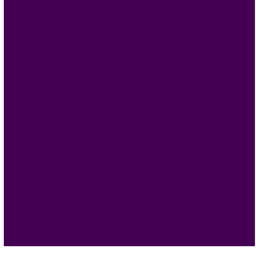
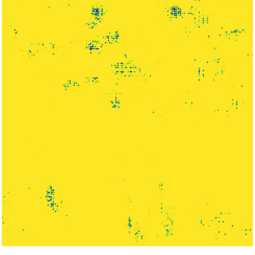
Generally, if only one PixelHop is used, we select several most discriminant channels for ensembles. If multiple PixelHops are used simultaneously, we select one to two most discriminant channels from each PixelHop for ensembles. All selections are based on the F1 score performance of the validation dataset.

3.4. Image-level decision ensemble

In the last stage, we ensemble predicted scores of all blocks in one image tile. Let N_{ch} denote the total number of selected channels. Since each channel has one predicted score from the previous step, each block has a feature vector of dimension N_{ch} . For each image, we concatenate the feature vectors of all blocks to form one feature vector of the image. Since there are 256 blocks in one tile. The dimension of the image-level feature vector is $256N_{ch}$. An XGBoost classifier is trained to determine the final prediction of each tile. N_{ch} is a hyperparameter that is decided by the performance of the validation dataset.

Table 1

Visualization of real and fake satellite images with heat maps, where cold and warm colors indicate a higher probability of being real and fake in the corresponding location, respectively.

Real		Fake	
Input image	Heat map	Input image	Heat map
			
			
			
			

3.5. Visualization of Detection Results

An attacker may stitch real/fake image blocks to form an image tile so as to confuse the ensemble classifier trained above. This can be addressed by providing a visualization tool to show the detection result in a local region. One example is given in Table 1. The table has four columns. The first two columns show four real images and their associated heat maps while the last two columns show four fake images and their associated heat maps. The color of local region in heat maps indicates the probability of being real or fake in that region. Cold and warm colors mean a higher probability of being real and fake, respectively. The heat map can be generated by averaging prediction scores of overlapping blocks with a smaller stride. To gain more insights, we show

channel-wise Saab features and channel-wise heat map for the DC, AC1, AC11 and AC26 frequencies of a PixelHop of dimension $3 \times 3 \times 3$ in Table 2, where DC and AC1 are low-frequency channels, AC11 is a mid-frequency channel and AC26 is a high-frequency channel. As shown in the last column of the table, DC and AC1 are not as discriminant as AC11 and AC26.

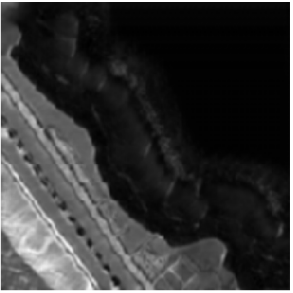
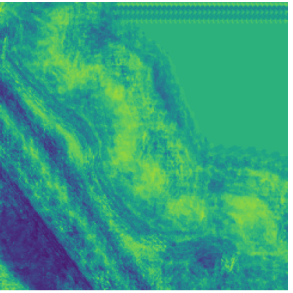
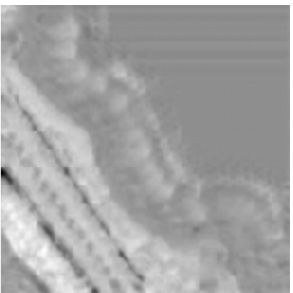
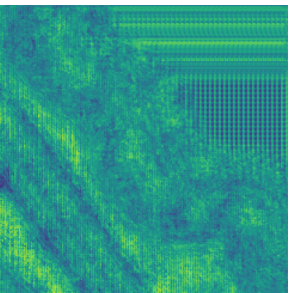
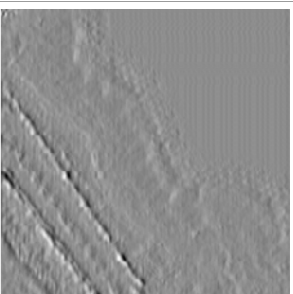
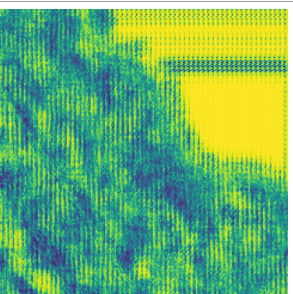
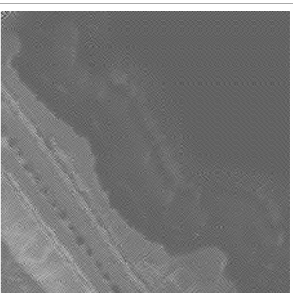
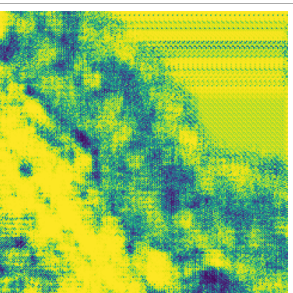
4. Experiments

4.1. Dataset

The UW Fake Satellite Image dataset (Zhao et al., 2021) is used to evaluate the proposed Geo-DefakeHop method.

Table 2

Visualization of absolute values of Saab filter responses and the detection heat maps for DC, AC1, AC11 and AC26 four channels, where DC and AC1 are low-frequency channels, AC11 is a mid-frequency channel, and AC26 is a high-frequency channel. Cold and warm colors in heat maps indicate a higher probability of being real and fake in the corresponding location, respectively.

Index	Name	Input image	Saab features	Heat map
0	DC			
1	AC1			
11	AC11			
26	AC26			

This is the first publicly available dataset targeting at authentic and fake satellite images detection. Its authentic satellite images are collected from Google Earth's satellite images while its fake satellite images are generated by CycleGAN. The base map used to generate fake satellite images are from CartoDB (CartoDB, 2021). There are 4032 authentic color satellite images of spatial resolution 256×256 and their fake counterparts in the dataset. It covers Tacoma, Seattle and Beijing three cities.

4.2. Experiment settings

We compare the performance of three methods: 1) the method proposed by Zhao *et al.* (Zhao *et al.*, 2021), 2) DefakeHop (Chen *et al.*, 2021), and 3) Geo-Defakehop. We follow the same experimental setting as given in (Zhao *et al.*, 2021). The dataset is randomly split into training (90%) and test sets (10%). The model is obtained by the training set and evaluated on the test set. In order to fine-tune hyperparameters, we further split 90% training images into

Table 3

Detection performance comparison with raw images from the UW dataset for three benchmarking methods. The boldface and the underbar indicate the best and the second-best results, respectively.

Method	Features or Designs	F1 score	Precision	Recall
Zhao, et al. (2021)	Spatial	75.81%	78.15%	73.61%
	Histogram	78.99%	72.93%	86.16%
	Frequency	65.84%	49.07%	100%
	Spatial + Histogram	86.77%	82.78%	91.17%
	Spatial + Frequency	77.02%	78.75%	75.36%
	Histogram + Frequency	83.90%	78.36%	90.29%
DefakeHop (2021)	Spatial + Histogram + Frequency	87.08%	82.73%	91.92%
Geo-DefakeHop (Ours)	PixelHop A	<u>99.88%</u>	100%	<u>99.75%</u>
	PixelHop B	100%	100%	100%
	PixelHop C	<u>99.88%</u>	100%	<u>99.75%</u>
	PixelHops A&B&C	100%	100%	100%

Table 4

Detection performance comparison for images resized from 256×256 to 128×128 and 64×64 . The boldface and the underbar indicate the best and the second-best results, respectively.

Tile size	Method	Features or Designs	F1 score	Precision	Recall
128 × 128	Zhao, et al. (2021)	Spatial	77.35%	76.61%	78.10%
		Histogram	80.09%	75.93%	84.72%
		Frequency	64.14%	47.21%	100%
		Spatial + Histogram	88.28%	85.81%	90.89%
		Spatial + Frequency	79.79%	81.38%	78.26%
		Histogram + Frequency	81.92%	76.99%	87.53%
	DefakeHop (2021)	Spatial + Histogram + Frequency	88.09%	86.52%	89.71%
	Geo-DefakeHop (Ours)	PixelHop A	100%	100%	100%
		PixelHop B	<u>99.88%</u>	100%	<u>99.75%</u>
		PixelHop C	99.75%	<u>99.75%</u>	<u>99.75%</u>
PixelHops A&B&C		100%	100%	100%	
64 × 64	Zhao, et al. (2021)	Spatial	76.46%	78.85%	74.21%
		Histogram	81.59%	76.60%	87.26%
		Frequency	49.75%	79.89%	36.12%
		Spatial + Histogram	88.22%	86.15%	90.39%
		Spatial + Frequency	77.46%	77.83%	77.09%
		Histogram + Frequency	83.16%	77.80%	89.32%
	DefakeHop (2021)	Spatial + Histogram + Frequency	87.91%	83.94%	92.29%
	Geo-DefakeHop (Ours)	PixelHop A	<u>98.27%</u>	<u>98.27%</u>	<u>98.27%</u>
		PixelHop B	97.39%	97.76%	97.03%
		PixelHop C	96.36%	97.71%	95.05%
PixelHops A&B&C		99.01%	99.01%	99.01%	

two parts: 80% for model training and 10% for the validation purpose. For Geo-DefakeHop, we consider four PixelHop designs:

- PixelHop A: Selected discriminant channels from 12 filters of dimension $2 \times 2 \times 3$,
- PixelHop B: Selected discriminant channels from 27 filters of dimension $3 \times 3 \times 3$,

- PixelHop C: Selected discriminant channels from 48 filters of dimension $4 \times 4 \times 3$,
- PixelHop A&B&C: Selected discriminant channels from PixelHops A, B and C.

We compare the detection performance under four settings:

- Raw images obtained from the UW dataset;
- Image tiles being resized from 256×256 to 128×128 and to 64×64 ;

Table 5

Detection performance comparison for images corrupted by additive white Gaussian noise with standard deviation $\sigma = 0.02, 0.06, 0.1$. The boldface and the underbar indicate the best and the second-best results, respectively.

Noise σ	Method	Features or Designs	F1 score	Precision	Recall
0.02	Zhao, et al. (2021)	Spatial	70.74%	72.58%	68.98%
		Histogram	81.24%	75.00%	88.60%
		Frequency	44.52%	67.66%	33.17%
		Spatial + Histogram	83.04%	82.41%	83.67%
		Spatial + Frequency	75.63%	78.42%	73.04%
		Histogram + Frequency	81.47%	76.62%	86.98%
	DefakeHop (2021)	Spatial + Histogram + Frequency	83.25%	81.47%	85.11%
			91.84%	93.75%	90.00%
	Geo-DefakeHop (Ours)	PixelHop A	97.56%	96.38%	98.77%
		PixelHop B	98.90%	98.05%	99.75%
PixelHop C		99.01%	98.53%	99.50%	
PixelHop A&B&C		98.65%	97.58%	99.75%	
0.06	Zhao, et al. (2021)	Spatial	68.22%	74.77%	62.72%
		Histogram	78.53%	71.70%	86.80%
		Frequency	65.39%	48.57%	100%
		Spatial + Histogram	80.74%	80.94%	80.54%
		Spatial + Frequency	76.39%	78.47%	74.42%
		Histogram + Frequency	80.28%	75.49%	85.71%
	DefakeHop (2021)	Spatial + Histogram + Frequency	81.42%	79.40%	83.55%
			92.78%	95.75%	90.00%
	Geo-DefakeHop (Ours)	PixelHop A	95.24%	93.98%	96.53%
		PixelHop B	96.59%	95.19%	98.02%
PixelHop C		95.07%	94.70%	97.28%	
PixelHop A&B&C		96.59%	95.19%	98.02%	
0.1	Zhao, et al. (2021)	Spatial	68.58%	69.76%	67.44%
		Histogram	77.13%	71.37%	83.91%
		Frequency	65.92%	78.48%	56.83%
		Spatial + Histogram	81.74%	78.42%	85.35%
		Spatial + Frequency	69.05%	70.35%	67.79%
		Histogram + Frequency	79.44%	74.67%	84.86%
	DefakeHop (2021)	Spatial + Histogram + Frequency	80.05%	77.78%	82.46%
			92.63%	97.78%	88.00%
	Geo-DefakeHop (Ours)	PixelHop A	94.43%	92.42%	96.53%
		PixelHop B	94.88%	93.51%	96.29%
PixelHop C		95.37%	93.99%	96.78%	
PixelHop A&B&C		96.10%	94.71%	97.52%	

- Image tiles corrupted additive white Gaussian noise with standard deviation $\sigma = 0.02, 0.06, 0.1$;
- Image tiles coded by the JPEG compression standard.

Training and test images go through the same image manipulation conditions. As to the performance metrics, we use the F1 score, precision and recall as defined by

$$\text{F1 score} = 2 \times \frac{\text{precision} \times \text{recall}}{\text{precision} + \text{recall}},$$

$$\text{precision} = \frac{\text{true positive}}{\text{true positive} + \text{false positive}},$$

$$\text{recall} = \frac{\text{true positive}}{\text{true positive} + \text{false negative}}.$$

4.3. Detection performance comparison

We compare the performance of three detection methods under various conditions in this subsection.

Raw images. We conduct both training and testing on raw images from the UW dataset (Zhao et al., 2021) and show the performance of the three methods in Table 3. As shown in the table, we see that PixelHop B and PixelHop A&B&C of Geo-DefakeHop achieve perfect detection performance with 100% F1 score, 100% precision and 100% recall while PixelHop A and PixelHop B achieve nearly perfect performance. Both Geo-DefakeHop and DefakeHop outperform Zhao *et al.*'s method in all performance metrics by significant margins. There is also a clear performance gap between Geo-DefakeHop and DefakeHop.

Image resizing. Image resizing is a common image manipulation operation. For the image tile of resolution 256×256 in the UW dataset, its scale with respect to the physical size is 1:8000. We resize the tile from 256×256 to images of lower resolutions (i.e. 128×128 and 64×64) and test the capability of the three methods in authentic/fake image detection. The results are shown in Table 4. For image resized to 128×128 , both PixelHop A and PixelHop A&B&C achieve perfect performance with 100% F1 score, 100% precision and 100% recall while PixelHop B and PixelHop C achieve nearly perfect performance. For image resized to 64×64 , we see the power of ensembles. That is, the F1 score, precision and recall of PixelHop A&B&C are all above 99%, which is slightly better than an individual PixelHop. Again, all four Geo-DefakeHop settings outperform Zhao *et al.*'s method by significant margins. DefakeHop is slightly better than Zhao *et al.*'s method but significantly worse than Geo-DefakeHop.

Additive white Gaussian noise. Satellite images can be corrupted by additive white Gaussian noise due to long distance image transmission or image acquisition. By normalizing the image pixel value to the range of $[0, 1]$, we test the detection performance with three noise levels $\sigma = 0.02, 0.06, 0.1$ and show the results in Table 5. We see from the table that, if authentic or fake satellite images are corrupted by white Gaussian noise with $\sigma = 0.02, 0.06$ and 0.1 , the F1 scores of Geo-DefakeHop decreases from 100% to 99.01%, 96.59% and 96.10%, respectively. In contrast, the F1 scores of DefakeHop are slightly above 90% and those of Zhao *et al.*'s method are around 80% or lower. Also, the ensemble gain of multiple PixelHops is more obvious as the noise level becomes higher.

JPEG compression. JPEG compression is commonly used for image sharing over the Internet. JPEG is a lossy compression method, where higher spatial frequencies are quantized by larger quantization step sizes. One can adjust the quality factor (QF) to get different trade offs between quality and coding bit rates. The QF value is between 0 and 1. The image has the best quality but the highest bit rate when QF is equal to 1. Typically, QF is chosen from the range of $[0.7, 1]$. In this experiment, we encode satellite images by JPEG with QF=0.95, 0.85 and 0.75 and investigate the robustness of benchmarking methods against these QF values. The results are shown in Table 6. The F1 scores of Geo-DefakeHop are 98.28%, 97.91% and 97.92% for QF=0.95, 0.85 and 0.75, respectively.

By comparing the three distortion types, the additive white Gaussian noise has the most negative impact on the detection performance, JPEG compression the second, and image resizing has the least impact. This is consistent with our intuition. Image resizing does not change the underlying information of images much, JPEG changes the information slightly because of the fidelity loss of high-frequencies and the additive white Gaussian noise perturbs the information of all frequencies.

4.4. Model size computation

For a PixelHop of filter size $s_1 \times s_2 \times c$, it has at most $M_{\max} = s_1 \times s_2 \times c$ filters. For example, the size of PixelHop A is $2 \times 2 \times 3$ and $M_{A,\max} = 12$. Similarly, we have $M_{B,\max} = 27$ and $M_{C,\max} = 48$. However, we choose only a subset of discriminant filters. They are denoted by M_A , M_B and M_C , respectively.

An XGBoost classifier consists of a sequence of binary decision trees, which are specified by two hyper-parameters: the max depth and the number of trees. Each XGBoost tree consists of both leaf nodes and non-leaf nodes. Non-leaf nodes have two parameters (i.e., the dimension and the value) to split the dataset where leaf nodes have one parameter (i.e., the predicted value). We have two types of XGBoost classifiers: 1) the channel-wise classifier and 2) the ensemble classifier. For the former, the max depth and the number of the trees are set to 1 and 100 respectively. Since each tree has one non-leaf node and two leaf nodes, its model size is $4 \times 100 = 400$ parameters. For the latter, the max depth and the number of trees are set to 1 and $100 \times M$, where $M = M_A + M_B + M_C$ is the total number of selected discriminant channels of all three PixelHops, respectively. The model size of the ensemble classifier is $4 \times 100 \times M = 400M$ parameters.

As an example, we provide the model size computation detail in Table 7 for four Geo-DefakeHop designs with the raw satellite images as the input. As shown in the table, PixelHops A, B, C and A&B&C have 812, 827, 848 and 2,487 parameters, respectively. Since the selected discriminant channel numbers of PixelHops A, B, C and A&B&C vary with raw, resized, noisy and compressed input satellite images, their model sizes are different. The model sizes are summarized in Table 8.

5. Conclusion and Future Work

A method called Geo-DefakeHop was proposed to distinguish between authentic and counterfeit satellite images. The design may contain a single PixelHop of different filter sizes or the ensemble of discriminant channels of multiple PixelHops. For the former, three design choices called PixelHop A, PixelHop B and PixelHop C were tested. For the latter, we considered a design by ensembles of discriminant channels of PixelHop A, PixelHop B and PixelHop C. The channel-wise performance analysis offers interpretability. The effectiveness of the Geo-DefakeHop method in terms of the F1 scores, precision and recall was demonstrated by extensive experiments. Furthermore, the model sizes of the four designs were thoroughly analyzed. They can be easily implemented in software on mobile or edge devices due to small model sizes.

The UW Fake Satellite Image dataset only contains Tacoma, Seattle and Beijing three cities. A large-scale fake satellite image dataset with more cities can be constructed to make the dataset more challenging. Besides, the current dataset was built by one GAN. One may build more fake satellite images with multiple GANs as well as computer graphics techniques. Furthermore, more manipulations such

Table 6

Detection performance comparison for images coded by the JPEG compression standard of three quality factors (QF), i.e., $QF = 95, 85$ and 75 . The boldface and the underbar indicate the best and the second-best results, respectively.

JPEG quality factor	Method	Features or Designs	F1 score	Precision	Recall	
95	Zhao, et al. (2021)	Spatial	74.88%	73.96%	75.82%	
		Histogram	76.05%	68.27%	85.83%	
		Frequency	64.37%	47.46%	100%	
		Spatial + Histogram	85.95%	82.49%	89.72%	
		Spatial + Frequency	78.00%	78.38%	77.62%	
		Histogram + Frequency	82.43%	74.95%	91.58%	
			Spatial + Histogram + Frequency	86.96%	85.06%	88.94%
		DefakeHop (2021)		98.00%	98.00%	98.00%
	Geo-DefakeHop (Ours)		PixelHop A	97.91%	97.31%	98.51%
			PixelHop B	97.90%	97.54%	98.27%
		PixelHop C	98.28%	97.56%	99.01%	
		PixelHop A&B&C	98.15%	97.55%	98.76%	
85	Zhao, et al. (2021)	Spatial	76.46%	78.64%	74.38%	
		Histogram	77.99%	72.71%	84.09%	
		Frequency	78.05%	75.85%	80.38%	
		Spatial + Histogram	85.91%	82.67%	89.42%	
		Spatial + Frequency	82.53%	81.48%	83.61%	
		Histogram + Frequency	85.28%	81.66%	89.24%	
			Spatial + Histogram + Frequency	89.54%	85.82%	93.6%
		DefakeHop (2021)		92.93%	93.88%	92.00%
	Geo-DefakeHop (Ours)		PixelHop A	97.54%	96.83%	98.27%
			PixelHop B	97.91%	97.08%	98.76%
		PixelHop C	97.91%	97.08%	98.76%	
		PixelHop A&B&C	97.54%	97.06%	98.02%	
75	Zhao, et al. (2021)	Spatial	73.88%	75.78%	72.03%	
		Histogram	80.96%	76.70%	85.71%	
		Frequency	80.77%	79.15%	82.47%	
		Spatial + Histogram	85.61%	81.70%	89.93%	
		Spatial + Frequency	87.09%	83.94%	90.49%	
		Histogram + Frequency	88.94%	87.41%	90.52%	
			Spatial + Histogram + Frequency	90.20%	88.46%	92.00%
		DefakeHop (2021)		94.85%	97.87%	92.00%
	Geo-DefakeHop (Ours)		PixelHop A	97.92%	96.63%	99.26%
			PixelHop B	97.66%	97.07%	98.27%
		PixelHop C	97.79%	96.84%	98.76%	
		PixelHop A&B&C	97.92%	96.63%	99.26%	

Table 7

Model size computation of four Geo-DefakeHop designs for raw satellite input images.

System	No. of Selected Channels	No. of Filter Parameters	No. of c/w XGBoost Parameters	No. of ensemble XGBoost Parameters	Total Model Size
Pixelhop A	1	12	400	400	812
Pixelhop B	1	27	400	400	827
Pixelhop C	1	48	400	400	848
Pixelhop A&B&C	3	87	1,200	1,200	2,487

as blurring and contrast adjustment can be added to test the limitation of the detection system.

6. Acknowledgments

This work was supported by the Army Research Laboratory (ARL) under agreement W911NF2020157.

Table 8

Summary of model sizes of four Geo-DefakeHop designs with different input images.

Experiments	PixelHop A	PixelHop B	PixelHop C	PixelHop A&B&C
Raw Images	0.8K	0.8K	0.8K	2.5K
Resizing	9.7K	20K	37K	61.7K
Noise	8.1K	13K	33K	38.5K
Compression	7.3K	19K	33K	37.4K

References

- Barni, M., Kallas, K., Nowroozi, E., Tondi, B., 2020. CNN detection of GAN-generated face images based on cross-band co-occurrences analysis, in: 2020 IEEE International Workshop on Information Forensics and Security (WIFS), IEEE, pp. 1–6.
- Brock, A., Donahue, J., Simonyan, K., 2018. Large scale GAN training for high fidelity natural image synthesis. arXiv preprint arXiv:1809.11096.
- CartoDB, 2021. <https://carto.com>.
- Chen, H.S., Rouhsedaghat, M., Ghani, H., Hu, S., You, S., Kuo, C.C.J., 2021. DefakeHop: A light-weight high-performance deepfake detector, in: 2021 IEEE International Conference on Multimedia and Expo (ICME), IEEE, pp. 1–6.
- Chen, T., Guestrin, C., 2016. Xgboost: A scalable tree boosting system, in: Proceedings of the 22nd acm sigkdd international conference on knowledge discovery and data mining, pp. 785–794.
- Chen, Y., Kuo, C.C.J., 2020. Pixelhop: A successive subspace learning (ssl) method for object recognition. Journal of Visual Communication and Image Representation 70, 102749.
- Choi, Y., Choi, M., Kim, M., Ha, J.W., Kim, S., Choo, J., 2018. StarGAN: Unified generative adversarial networks for multi-domain image-to-image translation, in: Proceedings of the IEEE conference on computer vision and pattern recognition, pp. 8789–8797.
- Dolhansky, B., Bitton, J., Pflaum, B., Lu, J., Howes, R., Wang, M., Ferrer, C.C., 2020. The deepfake detection challenge (dfdc) dataset. arXiv preprint arXiv:2006.07397.
- FBI, 2019. Protected voices: Foreign influence. <https://www.fbi.gov/video-repository/protected-voices-foreign-influence-102319.mp4/view>.
- Frank, J., Eisenhofer, T., Schönherr, L., Fischer, A., Kolossa, D., Holz, T., 2020. Leveraging frequency analysis for deep fake image recognition, in: International Conference on Machine Learning, PMLR, pp. 3247–3258.
- Guarnera, L., Giudice, O., Battiato, S., 2020. Deepfake detection by analyzing convolutional traces, in: Proceedings of the IEEE/CVF Conference on Computer Vision and Pattern Recognition Workshops, pp. 666–667.
- Hall, C.F., Hall, E.L., 1977. A nonlinear model for the spatial characteristics of the human visual system. IEEE Transactions on systems, man, and cybernetics 7, 161–170.
- Janowicz, K., Gao, S., McKenzie, G., Hu, Y., Bhaduri, B., 2020. GeoAI: spatially explicit artificial intelligence techniques for geographic knowledge discovery and beyond.
- Jiang, L., Li, R., Wu, W., Qian, C., Loy, C.C., 2020. Deepforensics-1.0: A large-scale dataset for real-world face forgery detection, in: Proceedings of the IEEE/CVF Conference on Computer Vision and Pattern Recognition, pp. 2889–2898.
- Karras, T., Aila, T., Laine, S., Lehtinen, J., 2017. Progressive growing of GANs for improved quality, stability, and variation. arXiv preprint arXiv:1710.10196.
- Karras, T., Laine, S., Aila, T., 2019. A style-based generator architecture for generative adversarial networks, in: Proceedings of the IEEE/CVF Conference on Computer Vision and Pattern Recognition, pp. 4401–4410.
- Kuo, C.C.J., Zhang, M., Li, S., Duan, J., Chen, Y., 2019. Interpretable convolutional neural networks via feedforward design. Journal of Visual Communication and Image Representation 60, 346–359.
- Li, Y., Yang, X., Sun, P., Qi, H., Lyu, S., 2020. Celeb-df: A large-scale challenging dataset for deepfake forensics, in: Proceedings of the IEEE/CVF Conference on Computer Vision and Pattern Recognition, pp. 3207–3216.
- Liu, X., Xing, F., Yang, C., Kuo, C.C.J., Babu, S., Fakhri, G.E., Jenkins, T., Woo, J., 2021. VoxelHop: Successive subspace learning for ALS disease classification using structural mri. arXiv preprint arXiv:2101.05131.
- Ma, L., Liu, Y., Zhang, X., Ye, Y., Yin, G., Johnson, B.A., 2019. Deep learning in remote sensing applications: A meta-analysis and review. ISPRS journal of photogrammetry and remote sensing 152, 166–177.
- Nataraj, L., Mohammed, T.M., Manjunath, B., Chandrasekaran, S., Flenner, A., Bappy, J.H., Roy-Chowdhury, A.K., 2019. Detecting GAN generated fake images using co-occurrence matrices. Electronic Imaging 2019, 532–1.
- Park, T., Liu, M.Y., Wang, T.C., Zhu, J.Y., 2019. Semantic image synthesis with spatially-adaptive normalization, in: Proceedings of the IEEE/CVF Conference on Computer Vision and Pattern Recognition, pp. 2337–2346.
- Radford, A., Wu, J., Child, R., Luan, D., Amodei, D., Sutskever, I., et al., 2019. Language models are unsupervised multitask learners. OpenAI blog 1, 9.
- Rössler, A., Cozzolino, D., Verdoliva, L., Riess, C., Thies, J., Nießner, M., 2018. Faceforensics: A large-scale video dataset for forgery detection in human faces. arXiv preprint arXiv:1803.09179.
- Wang, S.Y., Wang, O., Zhang, R., Owens, A., Efros, A.A., 2020. CNN-generated images are surprisingly easy to spot... for now, in: Proceedings of the IEEE/CVF Conference on Computer Vision and Pattern Recognition, pp. 8695–8704.
- Zhang, K., Wang, B., Wang, W., Sohrab, F., Gabbouj, M., Kuo, C.C.J., 2021. AnomalyHop: An SSL-based image anomaly localization method. arXiv preprint arXiv:2105.03797.
- Zhang, M., You, H., Kadam, P., Liu, S., Kuo, C.C.J., 2020. PointHop: An explainable machine learning method for point cloud classification. IEEE Transactions on Multimedia 22, 1744–1755.
- Zhang, X., Karaman, S., Chang, S.F., 2019. Detecting and simulating artifacts in GAN fake images, in: 2019 IEEE International Workshop on Information Forensics and Security (WIFS), IEEE, pp. 1–6.
- Zhao, B., Zhang, S., Xu, C., Sun, Y., Deng, C., 2021. Deep fake geography? When geospatial data encounter artificial intelligence. Cartography and Geographic Information Science 48, 338–352.
- Zhou, T., Wang, W., Liang, Z., Shen, J., 2021. Face forensics in the wild, in: Proceedings of the IEEE/CVF Conference on Computer Vision and Pattern Recognition, pp. 5778–5788.
- Zhu, J.Y., Park, T., Isola, P., Efros, A.A., 2017. Unpaired image-to-image translation using cycle-consistent adversarial networks, in: Proceedings of the IEEE international conference on computer vision, pp. 2223–2232.
- Zi, B., Chang, M., Chen, J., Ma, X., Jiang, Y.G., 2020. Wilddeepfake: A challenging real-world dataset for deepfake detection, in: Proceedings of the 28th ACM International Conference on Multimedia, pp. 2382–2390.